

6. Role of structural ordering on the radiation resistance response of $Gd_2Zr_2O_7$ pyrochlore

6.1 Introduction

Nuclear energy generates very low amount of carbon and other pollutants, and presently provides ~11% of the global electricity [2]. However, a variety of radioactive nuclear wastes are generated at the diverse phase of nuclear fuel processing (milling and mining of uranium ore, reactor operation, fuel fabrication, and used fuel reprocessing) in the nuclear power plants [2]. Therefore, there is a necessity for safe and effective management of these hazardous and environmentally sensitive high-level radioactive wastes (HLWs) [2,3].

Materials used for effective management of (involving their safe discharge and storage) radioactive wastes should be stable in radioactive environments. Therefore, the development of radiation-resistant compounds for the effective management of radioactive wastes is of utmost importance [1-3]. The scientific community all over the world is looking for appropriate materials for the secure disposal and effective management of radioactive wastes [3,4].

In recent years, the pyrochlore oxides are considered a promising host candidate for radionuclides waste immobilization because of their ability to easily accommodate the different types of actinides at crystallographic lattice sites [3-8]. Among the pyrochlore compounds, $Gd_2Zr_2O_7$ (GZO) is considered a suitable and promising host candidate for radioactive waste immobilization due to its exceptional chemical and thermal stability, radiation tolerance in hostile environments, mechanical properties, and so on [3,4,6,9,10]. GZO with $r_A/r_B = 1.46$ exhibited the order-disorder transformation instead of being amorphized upon irradiation with high energy heavy ions [11].

Here, we have focused on two major aspects of $Gd_2Zr_2O_7$ ceramic. First, we have demonstrated the structural ordering of $Gd_2Zr_2O_7$ enhanced with the increase of sintering temperature. Second, we have investigated the impact of different degrees of structural defects in the microsized $Gd_2Zr_2O_7$ on radiation tolerance using 100 MeV I^{7+} ions with the fluence of 1.0×10^{14} ions/cm² for possible nuclear applications. The materials, synthesis, and irradiation process of GZO are explained in chapter 2.

6.2 Results and Discussion

6.2.1 Structural and microstructural properties of GZO: Impact of sintering temperature

6.2.1.1 Structural and micro-structural analysis: XRD and FE-SEM

The presence of the superstructure reflections i.e., (111), (311), (331), (511), and (531) in the XRD patterns determine the crystal structure of pyrochlore compounds [12,13]. The detection of superstructure peaks in XRD patterns is typically difficult due to very weak reflections. Fig. 6. 1 (a-b) displays the XRD patterns of GZO pellet samples sintered at 1400°C and 1500°C for 48 h. The XRD pattern of the GZO14 and GZO15 exhibits the presence of pyrochlore superstructure reflections i.e., (111), (311), (331), (511), and (531). The appearance of the pyrochlore superstructure reflection characteristics is being evolved with sintering temperature in the GZO15 sample. The XRD pattern of the GZO15 sample shows the presence of all possible pyrochlore superstructure reflections [Fig. 6.1 (b)].

The presence of pyrochlore superstructure reflections in GZO14 and GZO15 samples exhibits the formation of the pyrochlore phase with the cubic crystal structure ($Fd\bar{3}m$). Pyrochlore structure is a superstructure derivative of fluorite structure (AO_2) with two different sites for A^{3+} and B^{4+} cations and three anion sites, i.e., 48f, 8a, and 8b. The more intense superstructure reflections of GZO15 sample with the increase of sintering temperature (1500°C) indicates that the degree of pyrochlore structural ordering increased with the increase of sintering temperature. These results show that the crystalline pyrochlore phase of the GZO system is being more ordered with the increase of sintering temperature, i.e., pyrochlore superstructural ordering enhances with sintering temperature. In other words, this is to say that the both samples, GZO14 and GZO15 possess different degree of ordering of pyrochlore phase [26-28].

The XRD results obtained here are in good agreement with previous studies [24-25,27]. Kong et al. have reported that the $Gd_2Zr_2O_7$ powder sample sintered at 1200°C for 12 h displays the disorder fluorite phase whereas the $Gd_2Zr_2O_7$ sintered at a similar temperature for the longer duration (50 h) exhibits the presence of superstructure reflections, i.e., pyrochlore phase formed upon heating for the longer time [13]. These results suggest that the fluorite-pyrochlore phase transition depends on both sintering temperature and time [13]. Further, they observed that the characteristics of the pyrochlore superstructure reflections of the $Gd_2Zr_2O_7$ system become more intense and sharp with the increase of sintering temperature from 1300° to 1400°C, and

stated that the induced degree of ordering in cation and anion sub-lattice increases significantly with the increase of sintering temperature, i.e., the ordering of pyrochlore phase increases with sintering temperature [13].

Zhou et al. [12] prepared the $Gd_2Zr_2O_7$ samples and sintered at various temperatures (300°C to 1600°C) to investigate the fluorite-pyrochlore-fluorite (F-P-F) phase transformation in $Gd_2Zr_2O_7$ system. They stated that the fluorite phase exist below 1250°C and fluorite-pyrochlore phase transition undergoes upon sintering within the range 1250°C to 1300°C. Upon sintering temperature of 1300°C to 1500°C, the ordering of pyrochlore phase take place and the degree of structural ordering enhanced as a function of sintering temperature. Interestingly, the pyrochlore structure transforms into a defective fluorite structure upon sintering above the temperature of 1550°C. The complete disappearance of the superstructure characteristics of $Gd_2Zr_2O_7$ ceramics upon sintering at 1600°C suggests the predominantly defective fluorite structure [12]. It should be noted that upon annealing above 1550°C, the pyrochlore structure transformed into a defective fluorite phase because thermal energy surpasses the cation defect formation energy and results in, both cations, the Gd^{3+} and Zr^{4+} in A-B sites become disordered.

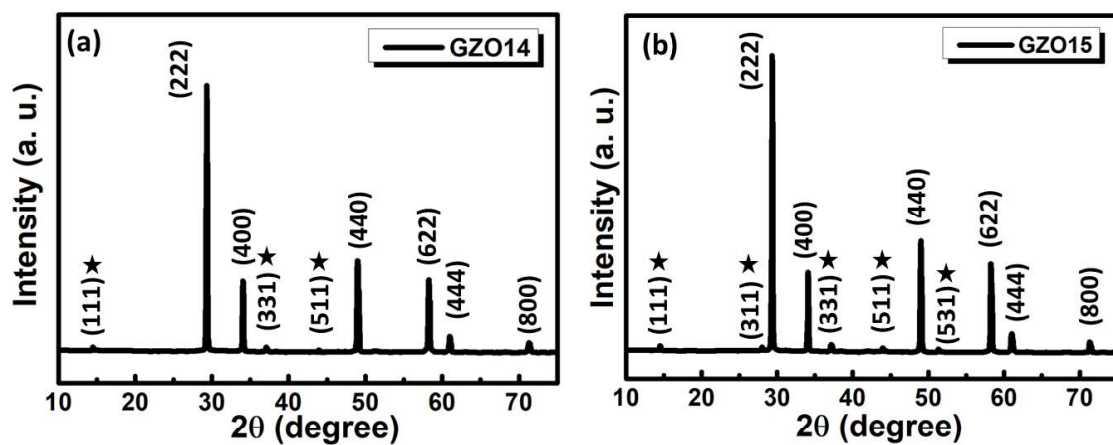


Figure 6.1 XRD patterns of GZO samples sintered at (a) 1400°C and (b) 1500°C.

Moreover, Zhang et al. have annealed the $Gd_2Zr_2O_7$ powder samples at various temperatures, i.e., 1100°C to 1550°C. It was observed that the degree of cationic ordering enhanced monotonically as a function of annealing temperature which suggests that the degree of structural ordering in the $Gd_2Zr_2O_7$ system depends on the annealing temperature [14]. Previous studies have revealed that the $Ln_2Zr_2O_7$ (Ln =rare earth) compounds experience fluorite-pyrochlore-fluorite phase transformation at specific temperatures [7,9,13–15]. Under ambient conditions, the ordered pyrochlore structure forms within cationic radii ratio, $1.46 < r_A/r_B < 1.78$ [7,14].

The smaller values of cationic radii ratio, $r_A/r_B < 1.46$, favored the formation of disordered fluorite phase [14].

Table 6.1 Displays the variation in the intensity of pyrochlore superstructure peaks in respect of (222) diffraction plane for GZO14 and GZO15 samples.

| Intensity (%) | 1400°C (GZO14) | 1500°C (GZO15) |
|-----------------------|-------------------|-------------------|
| $I_{(111)}/I_{(222)}$ | 2.01 | 2.48 |
| $I_{(331)}/I_{(222)}$ | 2.68 | 3.01 |
| $I_{(511)}/I_{(222)}$ | 1.63 | 1.86 |

With the cationic radii ratio of $r_A/r_B = 1.46$, the $Gd_2Zr_2O_7$ lies on the boundary of the pyrochlore and disordered fluorite phase. Therefore, the formation of disordered fluorite and/or pyrochlore phase $Gd_2Zr_2O_7$ is uncomplicated by engineering the cationic disordering/ordering at certain temperatures [12,24-26]. Using the peak profile fitting of GZO samples, we have measured the intensities of all diffraction planes. The variation in the ratio of the intensity of pyrochlore superstructure reflections, i.e., (111), (331), and (511) of GZO14 and GZO15 samples are displayed in table 1. It is noteworthy that the intensity of superstructure reflections relies on the induced degree of ordering/disordering, distribution of anion vacancies, and so on [2, 25].

Here, we wish to stress that the intensity of pyrochlore superstructure reflections in the GZO15 sample is found to be more prominent as compared to the GZO14 sample (Table 6.1). The variation of pyrochlore super-structural reflections indicates the relative enhancement in the pyrochlore phase ordering in the GZO15 sample. Therefore, we deduce that the degree of structural ordering relatively enhances from GZO14 to GZO15 samples with enhancing the sintering temperature and is in well agreement with earlier studies [12,13,15].

Fig. 6.2 (a-b) displays the variation in the intensity and FWHM of the most intense diffraction planes, i.e., (222), (400), (440), and (622) of GZO14 and GZO15 samples. Fig. 6.2 (a-b) gives evidence that the intensity of the diffraction planes increases and FWHM decreases with sintering temperature for the GZO15 sample. The enhancement in the intensity and decrement in the FWHM of GZO15 samples seem to be associated with the improvement of crystallinity and lattice strain due to enhanced sintering temperature [15,17,18].

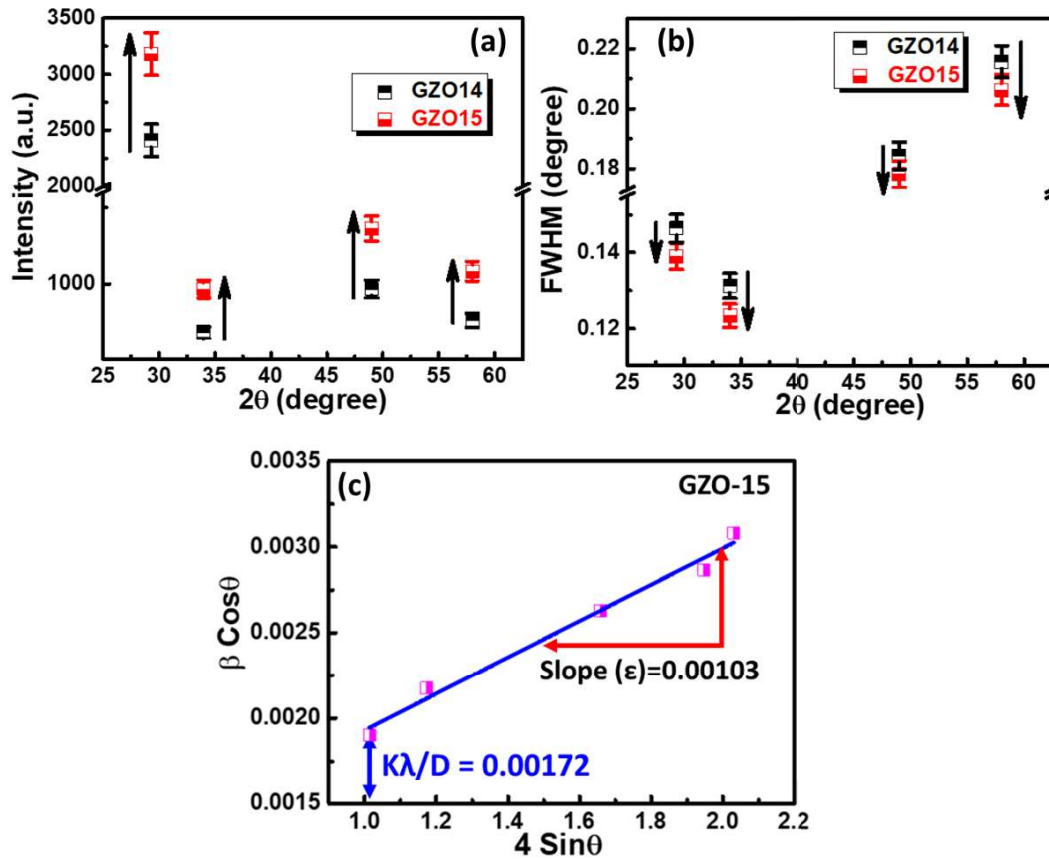


Figure 6.2 Variation in the intensity (a) and (b) FWHM of GZO14 and GZO15 samples upon sintering at 1400°C and 1500°C; and (c) Williamson-Hall plot of GZO15 sample.

The crystallite size and lattice strain of GZO samples were deduced employing the Williamson-Hall expression [19]

$$\beta_{hkl} \cos\theta = \frac{K\lambda}{D} + 4\epsilon \sin\theta \quad (6.1)$$

Where β_{hkl} , is the full width at half maximum (FWHM), D is crystallite size, ϵ is the lattice strain, λ is the wavelength, θ is the Bragg's angle, K is the dimensionless constant having a value of 0.94 for spherical crystals with cubic symmetry.

To obtain the values of peak positions and FWHM of the most intense reflections of the GZO samples, the whole pattern peak profile fitting was performed. The average crystallite size and lattice strain were deduced *via* a liner fitting between $\beta \cdot \cos\theta$ vs $4\sin\theta$ as shown in Fig. 6.2 (c). The calculated crystallite sizes from XRD analysis using W-H formalism were found to be 78.54 nm and 84.16 nm for GZO14 and GZO15 samples which seems well consistent with earlier studies [15,16].

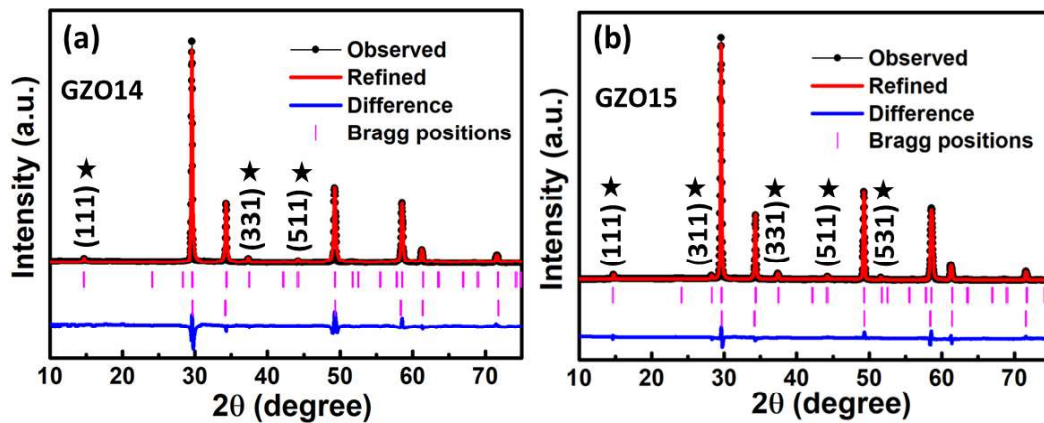


Figure 6.3 Rietveld refined XRD pattern of (a) GZO14 and (b) GZO15 samples. In Fig. (a-b) the top and bottom magenta color lines represent the peak positions for the pyrochlore and fluorite phase, respectively.

To get more insight into the lattice parameters and phase fraction, the Rietveld refinement of GZO samples has been performed using the FullProf program [20]. Fig. 6.3 displays the Rietveld refinement of GZO14 and GZO15 samples. XRD patterns of GZO samples were refined using the Pseudo-Voigt profile function. The refined lattice parameters of GZO14 and GZO15 are found to be 10.5336(2) Å to 10.5358(3) Å, respectively. Rietveld refinement of the GZO samples confirms that both samples possess the pyrochlore superstructure phase. It is found that the pyrochlore superstructure evolved with sintering temperature in the GZO15 sample.

The higher lattice parameter of the GZO15 sample as compared to the corresponding GZO14 sample seems to be associated with the enhanced structural ordering upon sintering at 1500°C [13,16]. Previous studies have also reported the enhancement in the lattice parameter of the $Gd_2Zr_2O_7$ system with the increase of annealing temperature [14], [15]. Similarly, Kaliyaperumal et al. have reported that the lattice parameter of the $Gd_2Zr_2O_7$ increases from 10.517 to 10.528 Å with the enhancement of sintering temperature (800 to 1400°C) [16]. The increase of lattice parameter suggests the expansion in the unit cell volume of GZO samples with the enhancement of sintering temperature which may be associated with the allocation of cations and oxygen ions in the respective sub-lattice, i.e., enhanced structural ordering with sintering temperature.

Table 6.2 provides the structural parameters deduced from the Rietveld refinement and W-H method for both GZO samples. As discussed above, the previous studies have demonstrated that the 1200°C and 1300°C are crucial points where fluorite to pyrochlore phase transition occurs [12]. It should be noted that the constitution of anion defects in pyrochlore

compounds has an inevitable effect on the emergence of defects in cation sub-lattice [14]. The researchers have also shown that the fluorite-pyrochlore phase transition depends on both, i.e., sintering time and temperature. Kong et al. [13] obtained the complete fluorite-pyrochlore phase transition upon sintering at 1200°C for 50 h which signifies that the fluorite-pyrochlore phase transition depends on both sintering temperature and time. Recently, Jafar et al. sintered the Gd₂Zr₂O₇ at different temperatures (1100°C, 1200°C, 1300°C, and 1400°C) and stated that pyrochlore phase ordering enhanced with sintering temperature.

The Gd₂Zr₂O₇ samples annealed at 1400°C exhibits an ordered pyrochlore structure [21]. The above-discussed results demonstrate that the annealing/sintering temperature induced the structural ordering/disordering in the pyrochlore compounds. Therefore, we wish to stress that the peak profile fitting analysis of XRD data and Rietveld refinement of GZO14 and GZO15 samples exhibit different degrees of structural ordering.

Table 6.2. Structural parameters (space group, lattice parameters, χ^2 , crystallite size, and lattice strain) were quantified from the Rietveld refinement and W-H plots of pyrochlore structure GZO samples.

| Temp. (°C) | Assigned sample code | Space group | Lattice parameter (Å) | χ^2 | Crystallite size (nm) | Lattice strain (%) |
|------------|----------------------|--------------|-----------------------|----------|-----------------------|--------------------|
| 1400 | GZO14 | $Fd\bar{3}m$ | 10.5336(2) | 1.72 | 78.54 | 0.103 |
| 1500 | GZO15 | $Fd\bar{3}m$ | 10.5358(1) | 1.51 | 84.16 | 0.092 |

Further, in order to obtain the impact of sintering temperature on the microstructure of sintered GZO samples, field emission scanning electron microscopy has been performed. Fig. 6.4 (a-b) displays the FE-SEM images of GZO14 and GZO15 samples. The average grain size is found to be 1.86±0.06 μm , and 2.76±0.08 μm for GZO14 and GZO15 samples, respectively. It should be noted that the grains and grain boundaries are more obvious for both samples.

The larger grains size of GZO15 reveals the coarsening phenomenon upon sintering at 1500°C. The coarsening phenomenon of small grains favored the grain growth, i.e., the grains size increased with the enhanced sintering temperature [20,22]. Therefore, the larger grain sizes of GZO15 samples seem to be attributed to thermal activated coarsening of small grains and curvature-driven diffusion/migration of grain boundaries at sintering of 1500°C [20]. The other earlier studies have also reported the similar grain growth of polycrystalline ceramics with enhanced sintering temperature [23,24].

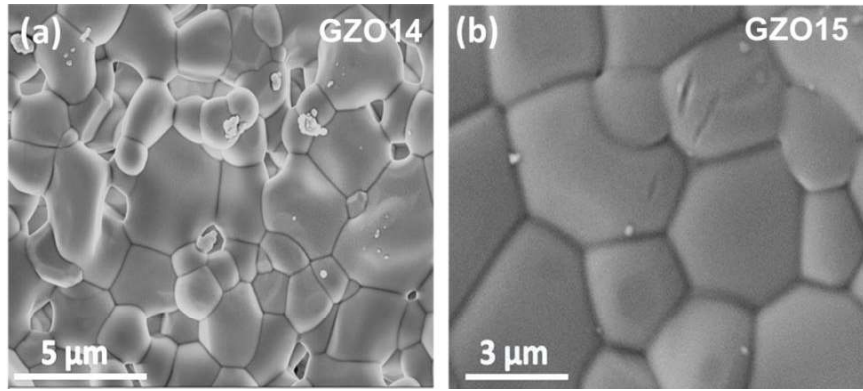


Figure 6.4 FE-SEM image of (a) GZO14 and (b) GZO15 samples sintered at 1400°C and 1500°C.

The theoretical density (ρ_{th}) of GZO14 and GZO15 samples was determined using the following expression [25].

$$\rho_{th} = \frac{8 \times 10^{24} M}{N_A a^3} \text{ g/cm}^3 \quad (6.2)$$

Where ' M ' is the molecular weight in g/mole, ' N_A ' is the Avogadro number, $6.02 \times 10^{23} \text{ mol}^{-1}$, and ' a ' is the lattice parameter (Å). The theoretical density (ρ_{th}) of the GZO15 samples decreases due to the enhancement of the unit cell parameters with the increase of sintering temperature. The relative density (ρ_r) of GZO samples was determined by employing the relation $\rho_r = (\rho/\rho_{th}) \%$. The relative density was found to be 94.56% and 95.87% for GZO14 and GZO15 samples which support the improved crystallinity and grain growth with sintering temperature. The earlier studies have also shown significant enrichment in the density of pyrochlore systems with the enhancement of sintering temperature [16,20]. Therefore, we wish to emphasize that the sintering temperature favored the grain growth and results in, grain size becomes bigger with the increase of sintering temperature.

6.2.1.2 Analysis of vibrational modes: Raman spectroscopy

Raman spectroscopy is perceptive to metal-oxygen vibrations and provides a complete understanding of short-range ordering/disordering in the lattice [13]. Conversely, XRD is more perceptive towards cation scattering, furnishes the information of cationic ordering/disordering [26]. Moreover, Raman spectroscopy explicitly quantifies the disordered fluorite, biphasic mixture, and ordered pyrochlore phase in $A_2B_2O_7$ compounds [26]. Therefore, Raman spectroscopy studies were conducted to investigate the impact of sintering temperature on structural characteristics, i.e., the degree of ordering/disordering of GZO samples.

The cubic pyrochlore structure compounds ($A_2B_2O_7$) with the space group $Fd\bar{3}m$ possess A_{1g} , E_g , and $4F_{2g}$ Raman active vibrational modes. The fluorite structure with the space

group of $Fm\bar{3}m$ exhibits solely one Raman active vibrational modes, i.e., F_{2g} [27]. Fig. 6.5 (a-b) displays the deconvoluted fitted Raman vibrational modes of GZO14 and GZO15 samples sintered at 1400°C and 1500°C, respectively. The assignment of the Raman vibrational modes varies for various pyrochlore compounds and Raman modes have been assigned based on the previous studies [26,28,29]. The Raman mode, E_g , situated at $\sim 319\text{ cm}^{-1}$ is attributed to O-Gd-O bending vibrations. Raman modes, A_{1g} , located at $\sim 519\text{ cm}^{-1}$ is originated from the stretching vibrations of Gd-O (48f).

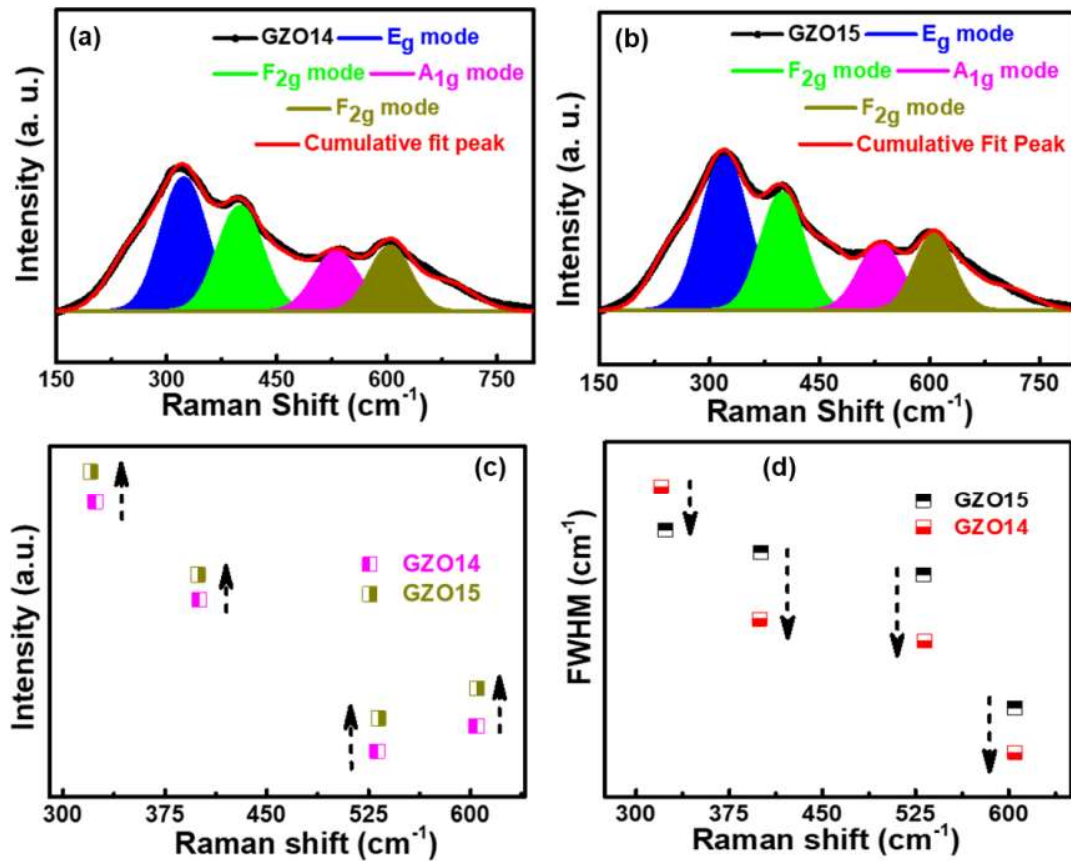


Figure 6.5 Deconvoluted Raman modes of (a) GZO14 and (b) GZO15 samples; (c-d) variation in the intensity and FWHM of Raman modes of GZO14 and GZO15 samples.

The two Raman modes, $2F_{2g}$ situated at ~ 401 and $\sim 598\text{ cm}^{-1}$ are attributed to the stretching vibrations of Zr-O (48f) and Gd-O (8a). The Raman spectra of GZO samples exhibit a substantial change with an increase of sintering temperature. As per the prediction of the group theory, the disappearance of vibrational modes (A_{1g} and E_g) in the Raman spectra specifies the transition from pyrochlore to disordered fluorite phase.

The group theory also specifies that the diminution of the number of F_{2g} mode commensurate the phase transformation from $Fd\bar{3}m$ to $Fm\bar{3}m$ [29]. Further, broadening in the Raman modes of the pyrochlore phase can be associated with structural disorder instead of

pyrochlore-fluorite phase transformation. Structural disordering in the pyrochlore compounds is an intrinsic phenomenon due to the presence of defects and vacancies. These defects and vacancies disrupt the symmetry of the lattice and result in, gives rise to broadened vibrational modes [3]. In the present study, the presence of vibrational modes (A_{1g} and E_g) in Raman spectra signifies the formation of pyrochlore structure of GZO samples, i.e., both GZO14 and GZO15 samples have pyrochlore structure ordering. Further, it was found that the intensity of the Raman modes ($E_g \sim 319$, $F_{2g} \sim 401$, $A_{1g} \sim 520$, and $F_{2g} \sim 598 \text{ cm}^{-1}$) increase with sintering temperature. Fig. 6 (c-d) illustrates the enhancement in the intensity and decrement in the FWHM of Raman vibrational modes with the increase of sintering temperature. Concurrently, augmentation of the intensity and decrement in the FWHM of vibrational modes of GZO samples indicate the enhancement in the ordering of anions sub-lattice. We wish to stress that the vibrational mode, A_{1g} ($\sim 520 \text{ cm}^{-1}$), which is correlated to the x-parameter of 48f oxygen (x_{48f}), evolves upon sintering at 1500°C and suggests the enhancement in degrees of the ordering of anions sub-lattice with the enrichment of sintering temperature.

Raman spectra of the $\text{Gd}_2\text{Zr}_2\text{O}_7$ system do not show sharp peaks as it is observed for the $\text{La}_2\text{Zr}_2\text{O}_7$ compound [30]. The line broadening in zirconate pyrochlore suggests a certain degree of disorder and the degree of disordering increases with the decrease of rare earth radius [31]. Therefore, the broad nature of the vibrational modes in the Raman spectra of GZO samples seems to be associated with the intrinsic disorder. Earlier studies have reported the fluorite to pyrochlore phase transformation upon sintering temperature at 1100°C to 1300°C with the enhancement of the structural ordering [10, 27, 29]. Kong et al. found that the Raman spectra of $\text{Gd}_2\text{Zr}_2\text{O}_7$ powder sample sintered at 1300°C exhibits the characteristics of the pyrochlore phase and pyrochlore phase become more evident as sintering temperature increases from 1300°C to 1400°C [13].

Zhou et al. stated that the $\text{Gd}_2\text{Zr}_2\text{O}_7$ system sintered below 1250°C exhibits the defect fluorite nature and defect fluorite to pyrochlore phase transition occurs within sintering temperature of 1250°C to 1300°C [12]. As sintering temperature increased from 1300°C to 1500°C , the degree of structural ordering increased, i.e., formed an ordered pyrochlore structure. Kaliyaperumal et al. stated that the $\text{Gd}_2\text{Zr}_2\text{O}_7$ powder annealed at 800°C possesses the pyrochlore structure and ordering of the pyrochlore phase enhances as a function of annealing temperature (1000 , 1200 , and 1400°C). Further, they stated that the vibrational modes, i.e., A_{1g} ($\sim 529 \text{ cm}^{-1}$) and F_{2g} (597 cm^{-1}) seem more evident and intense upon sintering at 1200°C and 1400°C , which specifies the enhancement in the pyrochlore phase ordering. The cumulative peak fitting of the Raman spectra indicates a substantial change in the vibrational

modes, i.e., the intensity of vibrational modes increases, and FWHM of vibrational modes decreases with sintering temperature in the GZO15 sample [Fig. 6.5 (c-d)].

These results signify that the GZO15 has a relatively some more extent of ordered pyrochlore structure due to enhancement of pyrochlore phase fraction with sintering temperature. Raman spectroscopy results discussed here are corroborated with XRD observations. Therefore, based on the above discussion, we deduce that both GZO samples possess a pyrochlore structure and the degree of an ordered pyrochlore phase is relatively higher in the GZO15 sample.

6.2.2 Impact of irradiation on sintered GZO: Radiation tolerance study

6.2.2.1 SRIM Simulation

The damage and implant depth profiles have been investigated using the SRIM 2013 [18] and are presented in Fig. 6.6. The ion irradiation damage distribution is found to be concentrated in the range of 7.2 to 10.5 μm [Fig. 6.6 (a)]. The simulated penetration depth for the sample is found to be 9.30 μm upon irradiation of 100 MeV I^{7+} ions. The variation of nuclear stopping power (S_n) and electronic stopping power (S_e) with target depth is calculated and presented in Fig. 6.6 (c). The simulated values of S_n and S_e for the GZO15 sample upon irradiation of 100 MeV I^{7+} ions are found to be 0.17 keV/nm and 20.10 keV/nm. The S_e is found to be nearly ~ 120 times higher than the corresponding S_n . It should be noted that the electronic energy loss phenomenon dominates for high energetic ions ($E > 50$ MeV) and the results presented here signify the predominance of the S_e than S_n .

6.2.2.2 Structural analysis: XRD studies of irradiated GZO samples

Structural order/disorder has a profound influence on the properties of materials. For example, structural disorder alters the photon transport in silicon photonic superlattice, electron transport in graphene, and heat transfer properties of the thermoelectric materials, and flux pinning in superconductors, and accordingly is used in various technological applications [32]. Structural order/disordered in pyrochlore compounds enhances electronic/ionic conductivity, catalytic activity in Li-O₂ batteries, and alters radiation tolerance (enhances the ability to immobilize the radioactive nuclides generated from used nuclear fuel) [32,33]. Sickafus et al. proposed that the oxide compounds, $\text{A}_2\text{B}_2\text{O}_7$, with pyrochlore and fluorite structures exhibit the inherent proclivity towards lattice disorder and are also well suitable to hindering lattice instability upon ion irradiation.

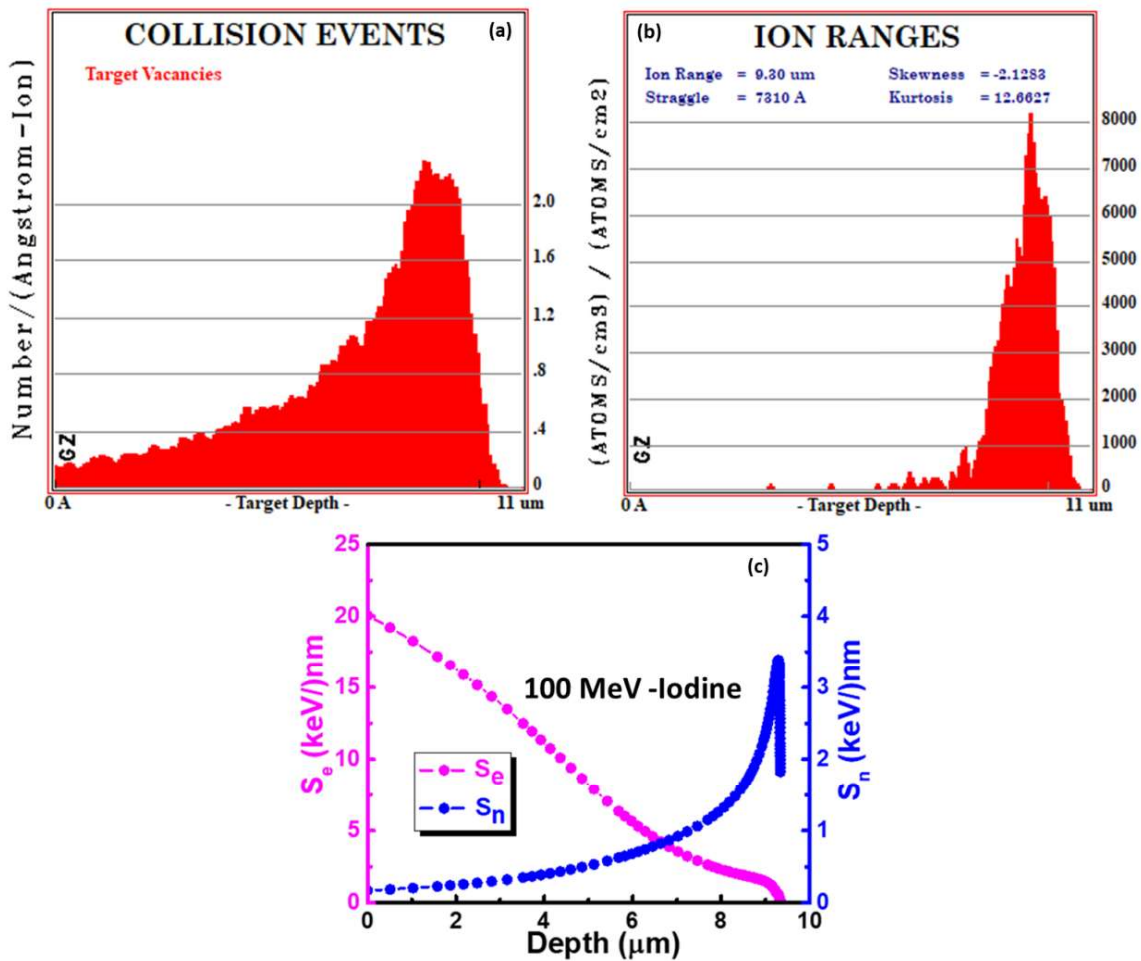


Figure 6.6 SRIM simulated collision events and ion ranges (a-b) and (c) variation of S_e and S_n as a function of depth of GZO15 sample.

Therefore, $A_2B_2O_7$ compounds with pyrochlore and fluorite structures are found to be suitable for the radiation-tolerant host for safe, effective management and reliable storage of radioactive wastes and surplus actinides [1]. The superior radiation resistance tolerance of $Gd_2Zr_2O_7$ proposes it as a promising candidate for the safe and effective management of radioactive nuclear waste [4]. In order to investigate the radiation tolerance of polycrystalline GZO14 and GZO15 samples, both samples were irradiated using 100 MeV I^{7+} ions with the fluence of 1.0×10^{14} ions/cm².

XRD patterns of ion irradiated GZO14 and GZO15 samples are shown in Fig. 6.7 (a-b). A substantial change in the XRD patterns of GZO14 and GZO15 samples is observed upon irradiation of 100 MeV iodine. The prudent evaluation of XRD patterns of irradiated GZO14 and GZO15 samples demonstrates the variation in the intensity and FWHM of the diffraction plans. The variation in the intensity and FWHM of GZO14 and GZO15 samples seems correlated with induced structural defects upon irradiation of iodine ions. It is found that the

broadening and weakening of XRD patterns of GZO14 are higher as compared to the corresponding GZO15 sample which indicates that the GZO15 sample possesses superior radiation resistance than GZO14 sample.

Moreover, the characteristics of superstructure reflections that represent pyrochlore structure are disappeared from both samples upon ion irradiation. Rietveld refinement of the pristine GZO14 and GZO15 samples display the pyrochlore phase structure [Fig. 6.3]. The disappearance of superstructure reflections from both GZO samples within XRD limits indicates irradiation-induced phase transformation from pyrochlore to disordered fluorite phase [34]. Patel et al. have reported the disappearance of pyrochlore superstructure reflections in the $Gd_2Zr_2O_7$ system upon irradiation of 90 MeV I and 120 MeV Au ions at the fluence of 1.0×10^{17} ions/cm² [8].

Sattonnay et al. [35] have irradiated the $Gd_2Zr_2O_7$ using 93 MeV Xe ions at different fluences and found that the weak pyrochlore superstructure reflections become disappear and reflections merely depict to fluorite structure has been observed at the fluence of 5.0×10^{12} ions/cm². They stated that ion irradiation induced an order-disorder transition in the $Gd_2Zr_2O_7$ system which results in, the anion deficient fluorite structure formed as a major phase due to random distribution of cations between A and B-sites. In another report, Sattonnay et al. reported that the $Gd_2Zr_2O_7$ system expressed the complete pyrochlore-fluorite transformation devoid of amorphization upon irradiation of swift heavy 870 MeV Xe ions at the fluence of 1.0×10^{13} ions/cm² [11].

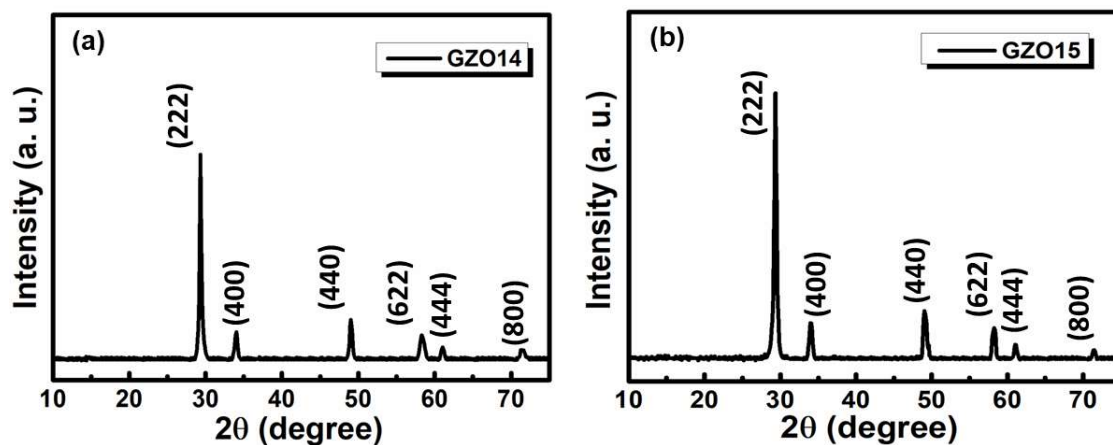


Figure 6.7 XRD patterns of (a) GZO14 and (b) GZO15 samples upon irradiation of 100 MeV I^{7+} at the fluence of 1.0×10^{14} ions/cm².

These results suggest that the $Gd_2Zr_2O_7$ favored the order-disorder transition instead of being amorphized. Moreover, Kumari et al. reported that the pyrochlore phase $Gd_2Zr_2O_7$ sample possess better crystallinity upon irradiation of 120 MeV Au at the fluence of 1.0×10^{14}

ions/cm², while the defect fluorite Gd₂Zr₂O₇ becomes amorphized, which specifies that the pyrochlore structure Gd₂Zr₂O₇ system has superior radiation resistance as compared to defective fluorite phase Gd₂Zr₂O₇ [36]. Gd₂Zr₂O₇ is formerly categorized as a relatively defective pyrochlore phase due to intrinsic cationic and anionic disordering in the respective sub-lattice [36]. In the present study, the XRD study unveils the order-disorder transition in both GZO samples upon ion irradiation. Earlier studies have reported similar observations and stated that the broadened and weakened XRD patterns in the Gd₂Zr₂O₇ system demonstrated induced disorder of cations at A and B sites upon ion irradiation [8,11,34].

Here, it should be noted that the pyrochlore structural ordering was found to be higher for GZO15 than the GZO14 sample. Therefore, the substantial changes in the intensity and FWHM of GZO14 and GZO15 samples upon ion irradiation seem to be associated with some extent of different degrees of structural ordering in pristine GZO samples. Therefore, we concluded that the superior radiation resistance of the GZO15 sample upon ion irradiation of 100 MeV I⁷⁺ ions may be associated with the extent degree of pyrochlore phase ordering in the GZO15 sample as compared to the corresponding GZO14 sample.

6.2.2.3 Analysis of vibrational modes: Raman spectroscopy studies of irradiated GZO samples

Through XRD analysis, the description of an apparent and accurate quantitative assessment of pyrochlore structure is challenging; because the emergence of weak superstructure reflections in the XRD patterns determined the pyrochlore structure of the system. As discussed above, the pyrochlore structure illustrates six Raman active modes, i.e., A_{1g}, E_g, and 4F_{2g}. The fluorite structure illustrates solely a single Raman active broad vibrational mode, i.e., F_{2g} [37]. Fig. 6.8 (a-b) illustrates the deconvoluted Raman spectra of GZO14 and GZO15 samples upon ion irradiation (account for the equivalent XRD patterns of GZO samples after irradiation in Fig. 6.7). Several studies have been performed to investigate the pyrochlore-fluorite phase transition in the zirconate pyrochlore compounds using the Raman spectroscopy [8,11,28,34,36,37].

The broadening, weakening, and disappearance of vibrational modes in the Raman spectra are related to induced structural defects, i.e., disordering in cation sub-lattice, anion sub-lattice, anion vacancies upon ion irradiation [36,38]. It is interesting to note that the qualitative assessment of the Raman spectra of GZO15 and GZO14 samples demonstrate the presence of E_g, A_{1g}, and 2F_{2g} vibrational modes. The presence of all possible vibrational modes signifies the presence of the pyrochlore phase in irradiated GZO samples. Kong et al. reported

that this type of broadened and weakened peaks was obtained for the disordered pyrochlore phase. We wish to stress that the XRD results of irradiated GZO samples did not show the pyrochlore superstructure reflections, the Raman spectroscopy analysis of irradiated GZO samples unambiguously endorses that both samples have pyrochlore structure. Here, it should be noted that the XRD is more suitable for detecting disorder in cation sub-lattice, while Raman spectroscopy is perceptible to metal-oxygen vibrational modes. Pokhrel et al. have reported that Raman spectroscopy studies of LaHfO and PrHfO compositions annealed at 1000°C signifies the phase transformation from defect fluorite to order pyrochlore phase, whereas XRD results did not exhibit the pyrochlore superstructure reflections [37].

The enriched disordering of cation and oxygen ions in the corresponding sub-lattice governs the pyrochlore-anion deficient defect fluorite phase transition [34]. It should be noted that the structural modifications in the zirconate pyrochlore are correlated to the composition of compounds upon irradiation [11,28,34]. Recently, the pyrochlore and defect fluorite phase $Gd_2Zr_2O_7$ has been irradiated using 100 MeV Au ions at different fluences (1.0×10^{12} ions/cm² to 1.0×10^{14} ions/cm²) [36]. The Raman spectroscopy performed on the pyrochlore and fluorite phase $Gd_2Zr_2O_7$ samples exhibited that the pyrochlore phase $Gd_2Zr_2O_7$ samples had better radiation tolerance as compared to corresponding fluorite phase $Gd_2Zr_2O_7$ samples [36]. This result signifies that the ordered pyrochlore phase $Gd_2Zr_2O_7$ possesses superior radiation stability over the defect fluorite $Gd_2Zr_2O_7$ phase. Further, it is an accepted trend that the enhancement in the intensity, and concurrently decrement in the FWHM of some vibrational modes, enhance the anion ordering in pyrochlore compounds [21].

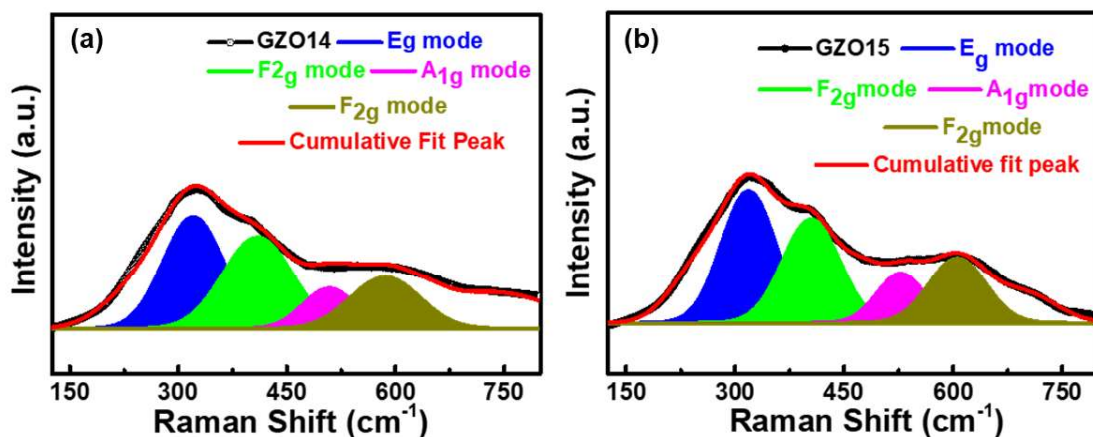


Figure 6.8 Deconvoluted Raman spectra of (a) GZO14 and (b) GZO15 upon irradiation of 100 MeV iodine ions.

In the present study, the accounted Raman spectra of GZO14 and GZO15 sample upon ion irradiation suggests the order-disorder transformation, i.e., pyrochlore to the fluorite phase

transition. However, the deconvoluted Raman spectra of both GZO14 and GZO15 samples exhibit the presence of E_g , A_{1g} , and $2F_{2g}$ vibrational modes. Consequently, in spite of enhanced disorder, the presence of these vibrational modes for both samples indicates the characteristic of pyrochlores, i.e., the weak pyrochlore type ordering which is well consistent with the earlier studies [16,36]. The pyrochlore and fluorite structures are correlated with the extent of ordering and disordering in the respective cationic and anionic sub-lattices and oxygen vacancies. $Gd_2Zr_2O_7$ lies at the borderline of fluorite and pyrochlore phase transformation due to the cationic radii ratio, $r_A/r_B=1.46$. Therefore, it is already considered as a disordered pyrochlore phase on account of the significant amount of cationic-anionic sub-lattice disordering and disordered oxygen vacancies [13].

As a result of enhanced disordered in cationic-anionic sub-lattice and oxygen vacancies, the $Gd_2Zr_2O_7$ system undergoes from pyrochlore to defect fluorite phase [36]. It is worth mentioning that the broadening of the Raman vibrational modes divulges the enhanced disorder upon ion irradiation. Hence, it would be pertinent to indicate that the ion irradiation further bolsters the disordering in GZO samples, and as a result, both GZO samples lead to a fluorite-type structure with weak pyrochlore ordering [36].

The attentive evaluation of deconvoluted Raman spectra of GZO14 and GZO15 samples demonstrate that the vibrational modes of the GZO14 sample are weaker and broader than the GZO15 sample comparatively. The relatively weaker and broader vibrational mode of the GZO14 sample signifies a higher loss of crystallinity (significant distortion in the vibrational modes) as compared to the corresponding GZO15 sample, i.e., ion irradiation generates relatively higher disorder in anionic sub-lattice in the GZO14 sample than GZO15. We wish to stress that the Raman spectroscopy results of GZO14 and GZO15 samples are consistent with XRD studies. Both, the XRD and Raman spectroscopy results exhibit that the GZO15 sample demonstrates better radiation tolerance as compared to the corresponding GZO14 sample. The variation in the structural modifications upon ion irradiation seems to be associated with different degrees of structural ordering in both GZO samples. The results discussed here suggest that the GZO samples with complex structures and possessing a tendency to accommodate lattice disorder are suitable to endure extremely high radiation resistance.

In accordance with preliminary calculations, experiments, and a variety of crystal structures ranging from pyrochlore to disordered fluorite structure, the $Gd_2Zr_2O_7$ oxide seems to be a promising candidate for hostile environments in the interest of safe and effective management of radioactive wastes and surplus actinides. In the present study, we demonstrated

the different degrees of structural ordering in GZO14 and GZO15 samples with the increase of sintering temperature. XRD and Raman's spectroscopy demonstrates that the GZO15 sample possesses better radiation tolerance than the GZO14 sample upon ion irradiation due to some extent ordered pyrochlore phase in the GZO15 sample (as quantified by Rietveld analysis).

The results presented here highlight the engineering of radiation tolerance from GZO14 to GZO15 which was found to be associated with the different degrees of structural ordering. Therefore, we concluded that the GZO samples presented here with different degrees of ordering/disordering could be suitable for applications in hostile environments, i.e., hosts materials for high-level radioactive waste and surplus actinides.

6.3 Conclusion

The impact of structural ordering/disordering on the radiation tolerance of GZO14 and GZO15 samples has been investigated employing characterization tools including XRD, FE-SEM, and Raman spectroscopy. The Rietveld refinement of GZO14 and GZO15 samples sintered at 1400°C and 1500°C demonstrates that both samples possess some different degrees of pyrochlore super-structural ordering. Raman spectroscopy studies also confirm the existence of the pyrochlore phase in both GZO samples and strengthen the Rietveld analysis. The different degrees of pyrochlore phase GZO14 and GZO15 samples were irradiated using 100 MeV I^{7+} ions at the fluence of 1.0×10^{14} ions/cm². Raman studies illustrate the presence of weak pyrochlore phase ordering while XRD analysis exhibited pyrochlore to fluorite phase transition upon irradiation. Both, the XRD and Raman spectroscopy studies exhibited that the GZO15 sample displays better radiation tolerance as compared to the GZO14 sample. The better radiation tolerance of the GZO15 sample seems associated with some extent of the ordered pyrochlore phase. The results reported here are appreciable as they may pave a path for the fabrication of complex oxide materials with different degrees of ordering/disordering for better radiation tolerance. Assessment of radiation resistance of GZO samples establishes the feasibility of it for the possible applications in hostile environments such as radiation tolerant hosts for safe and effective management of radioactive nuclear wastes and surplus actinides.

References

- [1] K.E. Sickafus, L. Minervini, R.W. Grimes, J.A. Valdez, M. Ishimaru, F. Li, K.J. McClellan, T. Hartmann, Radiation tolerance of complex oxides, *Science* (5480)289 (2000) 748–751. <https://doi.org/10.1126/science.289.5480.748>.
- [2] A. Pal, B.P. Mandal, K.A. Dubey, D. Jain, A. Bedar, A. Kumar, N. Goswami, B.C. Nailwal, B.N. Rath, A.K. Debnath, A.K. Singha, N.N. Kumar, R.D. Jain, A.K. Tyagi, R.C. Bindal, S. Kar, Polysulfone-Gd₂Zr₂O₇ mixed-matrix membranes with superior radiation resistant properties: Fabrication and application of a membrane device for radioactive effluent treatment, *Chem. Eng. J. Adv.* 1 (2020) 100006. <https://doi.org/10.1016/j.ceja.2020.100006>.
- [3] B.P. Mandal, M. Pandey, A.K. Tyagi, Gd₂Zr₂O₇ pyrochlore: Potential host matrix for some constituents of thorium based reactor's waste, *J. Nucl. Mater.* 406 (2010) 238–243. <https://doi.org/10.1016/j.jnucmat.2010.08.042>.
- [4] K. Liu, K. Zhang, T. Deng, J. Zeng, B. Luo, H. Zhang, Grain size effects on the aqueous durability of Gd₂Zr₂O₇ ceramics as high-level radioactive wastes matrix and its leaching mechanism, *Ceram. Int.* (2021) 1–11. <https://doi.org/10.1016/j.ceramint.2021.01.193>.
- [5] S.X. Wang, B.D. Begg, L.M. Wang, R.C. Ewing, W.J. Weber, K. V. Govidan Kutty, Radiation stability of gadolinium zirconate: A waste form for plutonium disposition, *J. Mater. Res.* 14 (1999) 4470–4473. <https://doi.org/10.1557/JMR.1999.0606>.
- [6] W.J. Weber, Plutonium Immobilization and Radiation Effects, *Science* (5487)289 (2000) 2051–2052. <https://doi.org/10.1126/science.289.5487.2051>.
- [7] K. Liu, K. Zhang, T. Deng, B. Luo, H. Zhang, Heavy-ion irradiation effects of Gd₂Zr₂O₇ nanocrystalline ceramics as nuclear waste immobilization matrix, *J. Nucl. Mater.* 538 (2020) 152236. <https://doi.org/10.1016/j.jnucmat.2020.152236>.
- [8] M.K. Patel, V. Vijayakumar, S. Kailas, D.K. Avasthi, J.C. Pivin, A.K. Tyagi, Structural modifications in pyrochlores caused by ions in the electronic stopping regime, *J. Nucl. Mater.* 380 (2008) 93–98. <https://doi.org/10.1016/j.jnucmat.2008.07.007>.
- [9] K. Liu, K. Zhang, T. Deng, W. Li, H. Zhang, Comparative study of irradiation effects on nanosized and microsized Gd₂Zr₂O₇ ceramics, *Ceram. Int.* 46 (2020) 16987–16992. <https://doi.org/10.1016/j.ceramint.2020.03.283>.
- [10] X. Lu, X. Shu, S. Chen, K. Zhang, F. Chi, H. Zhang, D. Shao, X. Mao, Heavy-ion irradiation effects on U₃O₈ incorporated Gd₂Zr₂O₇ waste forms, *J. Hazard. Mater.* 357 (2018) 424–430. <https://doi.org/10.1016/j.jhazmat.2018.06.026>.

- [11] G. Sattonnay, S. Moll, L. Thomé, C. Decorse, C. Legros, P. Simon, J. Jagielski, I. Jozwik, I. Monnet, Phase transformations induced by high electronic excitation in ion-irradiated $\text{Gd}_2(\text{Zr}_x\text{Ti}_{1-x})_2\text{O}_7$ pyrochlores, *J. Appl. Phys.* 108 (2010) 103512. <https://doi.org/10.1063/1.3503452>.
- [12] L. Zhou, Z. Huang, J. Qi, Z. Feng, D. Wu, W. Zhang, X. Yu, Y. Guan, X. Chen, L. Xie, K. Sun, T. Lu, Thermal-Driven Fluorite–Pyrochlore–Fluorite Phase Transitions of $\text{Gd}_2\text{Zr}_2\text{O}_7$ Ceramics Probed in Large Range of Sintering Temperature, *Metall. Mater. Trans. A.* 47 (2016) 623–630. <https://doi.org/10.1007/s11661-015-3234-4>.
- [13] L. Kong, I. Karatchevtseva, D.J. Gregg, M.G. Blackford, R. Holmes, G. Triani, $\text{Gd}_2\text{Zr}_2\text{O}_7$ and $\text{Nd}_2\text{Zr}_2\text{O}_7$ pyrochlore prepared by aqueous chemical synthesis, *J. Eur. Ceram. Soc.* 33 (2013) 3273–3285. <https://doi.org/10.1016/j.jeurceramsoc.2013.05.011>.
- [14] F.X. Zhang, M. Lang, R.C. Ewing, Atomic disorder in $\text{Gd}_2\text{Zr}_2\text{O}_7$ pyrochlore, *Appl. Phys. Lett.* 106 (2015) 191902. <https://doi.org/10.1063/1.4921268>.
- [15] Y.H. Lee, H.S. Sheu, J.P. Deng, H.-C.I. Kao, Preparation and fluorite–pyrochlore phase transformation in $\text{Gd}_2\text{Zr}_2\text{O}_7$, *J. Alloys Compd.* 487 (2009) 595–598. <https://doi.org/10.1016/j.jallcom.2009.08.021>.
- [16] C. Kaliyaperumal, A. Sankarakumar, T. Paramasivam, Grain size effect on the electrical properties of nanocrystalline $\text{Gd}_2\text{Zr}_2\text{O}_7$ ceramics, *J. Alloys Compd.* 813 (2020). <https://doi.org/10.1016/j.jallcom.2019.152221>.
- [17] Y. Kumar, P.M. Shirage, Highest coercivity and considerable saturation magnetization of CoFe_2O_4 nanoparticles with tunable band gap prepared by thermal decomposition approach, *J. Mater. Sci.* 52 (2017) 4840–4851. <https://doi.org/10.1007/s10853-016-0719-5>.
- [18] A. Panghal, Y. Kumar, P.K. Kulriya, P.M. Shirage, N.L. Singh, Structural assessment and irradiation response of $\text{La}_2\text{Zr}_2\text{O}_7$ pyrochlore: Impact of irradiation temperature and ion fluence, *J. Alloys Compd.* 862 (2021) 158556. <https://doi.org/10.1016/j.jallcom.2020.158556>.
- [19] Y. Kumar, A.K. Rana, P. Bhojane, M. Pusty, V. Bagwe, S. Sen, P.M. Shirage, Controlling of ZnO nanostructures by solute concentration and its effect on growth, structural and optical properties, *Mater. Res. Express.* 2 (2015) 105017. <https://doi.org/10.1088/2053-1591/2/10/105017>.
- [20] A. Panghal, P.K. Kulriya, Y. Kumar, F. Singh, N.L. Singh, Investigations of atomic disorder and grain growth kinetics in polycrystalline $\text{La}_2\text{Zr}_2\text{O}_7$, *Appl. Phys. A Mater. Sci. Process.* 125 (2019) 1–11. <https://doi.org/10.1007/s00339-019-2720-8>.

- [21] M. Jafar, S.B. Phapale, B.P. Mandal, M. Roy, S.N. Achary, R. Mishra, A.K. Tyagi, Effect of temperature on phase evolution in $Gd_2Zr_2O_7$: A potential matrix for nuclear waste immobilization, *J. Alloys Compd.* 867 (2021) 159032. <https://doi.org/10.1016/j.jallcom.2021.159032>.
- [22] P.K. Kulriya, T. Yao, S.M. Scott, S. Nanda, J. Lian, Influence of grain growth on the structural properties of the nanocrystalline $Gd_2Ti_2O_7$, *J. Nucl. Mater.* 487 (2017) 373–379. <https://doi.org/10.1016/j.jnucmat.2017.02.032>.
- [23] A. Panghal, P.K. Kulriya, Y. Kumar, F. Singh, N.L. Singh, Investigations of atomic disorder and grain growth kinetics in polycrystalline $La_2Zr_2O_7$, *Appl. Phys. A.* 125 (2019) 428. <https://doi.org/10.1007/s00339-019-2720-8>.
- [24] N.F. Syamimi, K. Amin Matori, W.F. Lim, S. Abdul Aziz, M.H. Mohd Zaid, Effect of Sintering Temperature on Structural and Morphological Properties of Europium (III) Oxide Doped Willemite, *J. Spectrosc.* 2014 (2014) 1–8. <https://doi.org/10.1155/2014/328931>.
- [25] Y. Kumar, A. Sharma, P.M. Shirage, Impact of different morphologies of $CoFe_2O_4$ nanoparticles for tuning of structural, optical and magnetic properties, *J. Alloys Compd.* 778 (2019) 398–409. <https://doi.org/10.1016/j.jallcom.2018.11.128>.
- [26] B.P. Mandal, P.S.R. Krishna, A.K. Tyagi, Order–disorder transition in the $Nd_{2-y}Y_yZr_2O_7$ system: Probed by X-ray diffraction and Raman spectroscopy, *J. Solid State Chem.* 183 (2010) 41–45. <https://doi.org/10.1016/j.jssc.2009.10.010>.
- [27] M. Glerup, O.F. Nielsen, F.W. Poulsen, The Structural Transformation from the Pyrochlore Structure, $A_2B_2O_7$, to the Fluorite Structure, AO_2 , Studied by Raman Spectroscopy and Defect Chemistry Modeling, *J. Solid State Chem.* 160 (2001) 25–32. <https://doi.org/10.1006/jssc.2000.9142>.
- [28] B.P. Mandal, N. Garg, S.M. Sharma, A.K. Tyagi, Solubility of ThO_2 in $Gd_2Zr_2O_7$ pyrochlore: XRD, SEM and Raman spectroscopic studies, *J. Nucl. Mater.* 392 (2009) 95–99. <https://doi.org/10.1016/j.jnucmat.2009.03.050>.
- [29] N.J. Hess, B.D. Begg, S.D. Conradson, D.E. McCready, P.L. Gassman, W.J. Weber, Spectroscopic Investigations of the Structural Phase Transition in $Gd_2(Ti_{1-y}Zr_y)_2O_7$ Pyrochlores, *J. Phys. Chem. B.* 106 (2002) 4663–4677. <https://doi.org/10.1021/jp014285t>.
- [30] D. Michel, M.P. y Jorba, R. Collongues, Study by Raman spectroscopy of order-disorder phenomena occurring in some binary oxides with fluorite-related structures, *J. Raman Spectrosc.* 5 (1976) 163–180. <https://doi.org/10.1002/jrs.1250050208>.

- [31] B.E. SCHEETZ, W.B. WHITE, Characterization of Anion Disorder in Zirconate $A_2B_2O_7$ Compounds by Raman Spectroscopy, *J. Am. Ceram. Soc.* 62 (1979) 468–470. <https://doi.org/10.1111/j.1151-2916.1979.tb19107.x>.
- [32] J. Shamblin, M. Feygenson, J. Neuefeind, C.L. Tracy, F. Zhang, S. Finkeldei, D. Bosbach, H. Zhou, R.C. Ewing, M. Lang, Probing disorder in isometric pyrochlore and related complex oxides, *Nat. Mater.* 15 (2016) 507–511. <https://doi.org/10.1038/nmat4581>.
- [33] J. Lian, L.M. Wang, S.X. Wang, J. Chen, L.A. Boatner, R.C. Ewing, Nanoscale manipulation of pyrochlore: New nanocomposite ionic conductors, *Phys. Rev. Lett.* 87 (2001) 3–6. <https://doi.org/10.1103/PhysRevLett.87.145901>.
- [34] M. Lang, F.X. Zhang, R.C. Ewing, J. Lian, C. Trautmann, Z. Wang, Structural modifications of $Gd_2Zr_{2-x}Ti_xO_7$ pyrochlore induced by swift heavy ions: Disordering and amorphization, *J. Mater. Res.* 24 (2009) 1322–1334. <https://doi.org/10.1557/jmr.2009.0151>.
- [35] G. Sattonnay, L. Thomé, N. Sellami, I. Monnet, C. Grygiel, C. Legros, R. Tetot, Phase transformations in pyrochlores irradiated with swift heavy ions: Influence of composition and chemical bonding, *Acta Phys. Pol. A.* 123 (2013) 862–866. <https://doi.org/10.12693/APhysPolA.123.862>.
- [36] R. Kumari, P.K. Kulriya, V. Grover, R. Shukla, K. Saravanan, S. Mohapatra, A.K. Tyagi, D.K. Avasthi, Radiation stability of $Gd_2Zr_2O_7$: Effect of stoichiometry and structure, *Ceram. Int.* 42 (2016) 103–109. <https://doi.org/10.1016/j.ceramint.2015.08.007>.
- [37] M. Pokhrel, S.K. Gupta, K. Wahid, Y. Mao, Pyrochlore Rare-Earth Hafnate $RE_2Hf_2O_7$ (RE=La and Pr) Nanoparticles Stabilized by Molten-Salt Synthesis at Low Temperature, *Inorg. Chem.* 58 (2019) 1241–1251. <https://doi.org/10.1021/acs.inorgchem.8b02728>.
- [38] M.K. Patel, V. Vijayakumar, D.K. Avasthi, S. Kailas, J.C. Pivin, V. Grover, B.P. Mandal, A.K. Tyagi, Effect of swift heavy ion irradiation in pyrochlores, *Nucl. Instruments Methods Phys. Res. Sect. B Beam Interact. with Mater. Atoms.* 266 (2008) 2898–2901. <https://doi.org/10.1016/j.nimb.2008.03.135>.